Research Article

Nano Research
2023, 16(8): 10796–10802

ISSN 1998-0124 CN 11-5974/O4
https://doi.org/10.1007/s12274-023-5859-8

The d-orbital regulation of isolated manganese sites for enhanced oxygen evolution

Xue Bai[1], Jingyi Han[1], Xiaodi Niu[2] (✉), and Jingqi Guan[1] (✉)

[1] *Institute of Physical Chemistry, College of Chemistry, Jilin University, 2519 Jiefang Road, Changchun 130021, China*
[2] *College of Food Science and Engineering, Jilin University, Changchun 130062, China*

Received: 14 April 2023 / **Revised:** 5 May 2023 / **Accepted:** 19 May 2023

ABSTRACT

Developing transition metal-nitrogen-carbon materials (M-N-C) as electrocatalysts for the oxygen evolution reaction (OER) is significant for low-cost energy conversion systems. Further d-orbital adjustment of M center in M-N-C is beneficial to the improvement of OER performance. Herein, we synthesize a single-Mn-atom catalyst based on carbon skeleton (Mn_1-$N_2S_2C_x$) with isolated Mn-N_2S_2 sites, which exhibits high alkaline OER activity (η_{10} = 280 mV), low Tafel slope (44 mV·dec^{-1}), and excellent stability. Theoretical calculations reveal the pivotal function of isolated Mn-N_2S_2 sites in promoting OER, including the adsorption kinetics of intermediates and activation mechanism of active sites. The doping of S causes the increase in both charge density and work function of active Mn center, and ortho-Mn_1-$N_2S_2C_x$ expresses the fastest OER kinetics due to the asymmetric plane.

KEYWORDS

dual-heteroatom coordination, Mn_1-$N_2S_2C_x$, oxygen evolution reaction (OER), single-atom catalyst, theoretical calculation

1 Introduction

Electrocatalytic water splitting and fuel cell industrialization are effective strategies for the conversion and storage of electric energy, attracting wide attention because of their green and sustainable development characteristics [1–5]. As an important semi-reaction of water splitting, the low efficiency of oxygen evolution reaction (OER) is an urgent problem to be solved, which dominates the efficiency of energy conversion [6, 7]. Although noble-metal-based electrocatalysts show outstanding advancement to overcome the high reaction kinetics caused by the four-electron transfer of OER, they lack long-term development due to the high cost [8, 9]. Therefore, more sustainable and earth-abundant electrocatalysts need to be explored in order to cope with the foreseeable energy crisis.

Single-atom transition metal catalysts, with highly exposed active sites and close to 100% atom utilization, have stood out from other materials as promising alternatives to precious metal catalysts [10–14]. Iron- and cobalt-base single atom catalysts (SACs) have been widely studied, which can display comparable OER catalytic activity with IrO_2, but they are less stable at high voltages [15, 16]. Further, manganese fulfills the requirements of environmental protection and is abundantly available in the Earth's crust. It serves as a natural OER active species, giving it an inherent advantage over iron or cobalt [17, 18]. Due to the abundant valence, manganese can have timely electron transfer with oxygen intermediates during the reaction, which is conducive to the activation of Mn species. However, research on the electrocatalytic performance of isolated Mn sites is extremely limited, which is meaningful but challenging to develop Mn-based single-atom catalysts with high OER activity.

The OER activity of SACs is derived from the adsorption and desorption ability of the central metal atom to oxygen intermediates. Therefore, it is a meaningful research direction to precisely control and adjust the local environment of isolated metal atoms in order to obtain the right bonding strength with oxygen intermediates. In the classical carbon-based N-doped SACs (M-N-C), transition metal atoms are usually anchored with four N atoms to form a stable M-N_4 active plane for the OER [19, 20]. The presence of N atom not only increases the intrinsic catalytic activity of carbon substrate, but also enhances the metal-support interaction and accelerates the electron transfer. Introducing axial ligands is a strategy to adjust the d orbital of central M by destroying the plane geometry of M-N_x. Li et al. used ZIF-8 as a precursor to introduce imidazole rings onto Fe-N_4 and synthesized Fe-N_5 with five N-atom-coordination structures and asymmetric electron depletion region, promoting the formation of OER active intermediates [21]. However, the ligands are easy to lose, causing catalyst deactivation [22]. Furthermore, theoretical calculations have demonstrated that the doping of other heteroatoms for M-N-C causes unexpected improvements in terms of reducing the activation energy of the reaction [23, 24]. The introduction of oxygen can change the reactivity of M-N-C by altering the electronic state near the Fermi level [25, 26]. Since the electronegativity of S is close to carbon, the introduction of S causes less charge rearrangement on carbon materials than other heteroatoms, and the spin density redistribution induced by S is more conducive to fine-tuning of electronic structure [27, 28]. Inspired by this, we regulated the d-electron structure of Mn by changing the coordination ratio of nitrogen and sulfur to obtain better OER activity.

Address correspondence to Xiaodi Niu, niuxd@jlu.edu.cn; Jingqi Guan, guanjq@jlu.edu.cn

Here, we adopted a regulation strategy for electronic structure of Mn via S-/N-co-doping to achieve excellent OER activity. Single-atom Mn catalyst Mn_1-$N_2S_2C_x$ with nitrogen and sulfur coordination was obtained by a one-step high temperature annealing method. The catalyst demonstrated excellent OER activity under alkaline conditions, with an overpotential of 280 mV and a Tafel slope of 44 mV·dec^{-1}, which is superior to most previously reported Mn-based electrocatalysts and commercial iridium dioxide. X-ray absorption spectra (XAS) and theoretical calculations reveal that the doping of S and the presence of an asymmetric structure contribute to the ortho-Mn_1-$N_2S_2C_x$ having the lowest OER reaction barrier, with the rate-limiting step being the conversion of O* → OOH*. The work demonstrates that the importance of doping S for tuning the d orbit of M in M-N-C, which promotes the development of high-performance OER electrocatalysts.

2 Results and discussion

2.1 Characterization of single-atom Mn catalysts

We synthesized a single manganese atomic electrocatalyst Mn_1-$N_2S_2C_x$ by simple high-temperature calcination, where manganese is co-coordinated with nitrogen and sulfur and located on graphene (Fig. 1(a)). The Mn^{2+} ions were uniformly absorbed onto graphene oxide nanosheets by ultrasound and freeze-dried treatment. Under high temperature annealing, sulfur from cosan and nitrogen from the decomposition of melamine were doped into the mixture and coordinated to the Mn sites to form Mn_1-$N_2S_2C_x$. Moreover, the graphene oxide was transformed into N- and S-codoped graphene. Simultaneously, Mn-based single-atom catalysts containing nitrogen, sulfur, and no heteroatomic coordination were synthesized for comparative study, which are named as Mn-SC, Mn-NC, and Mn-C, respectively. The structure

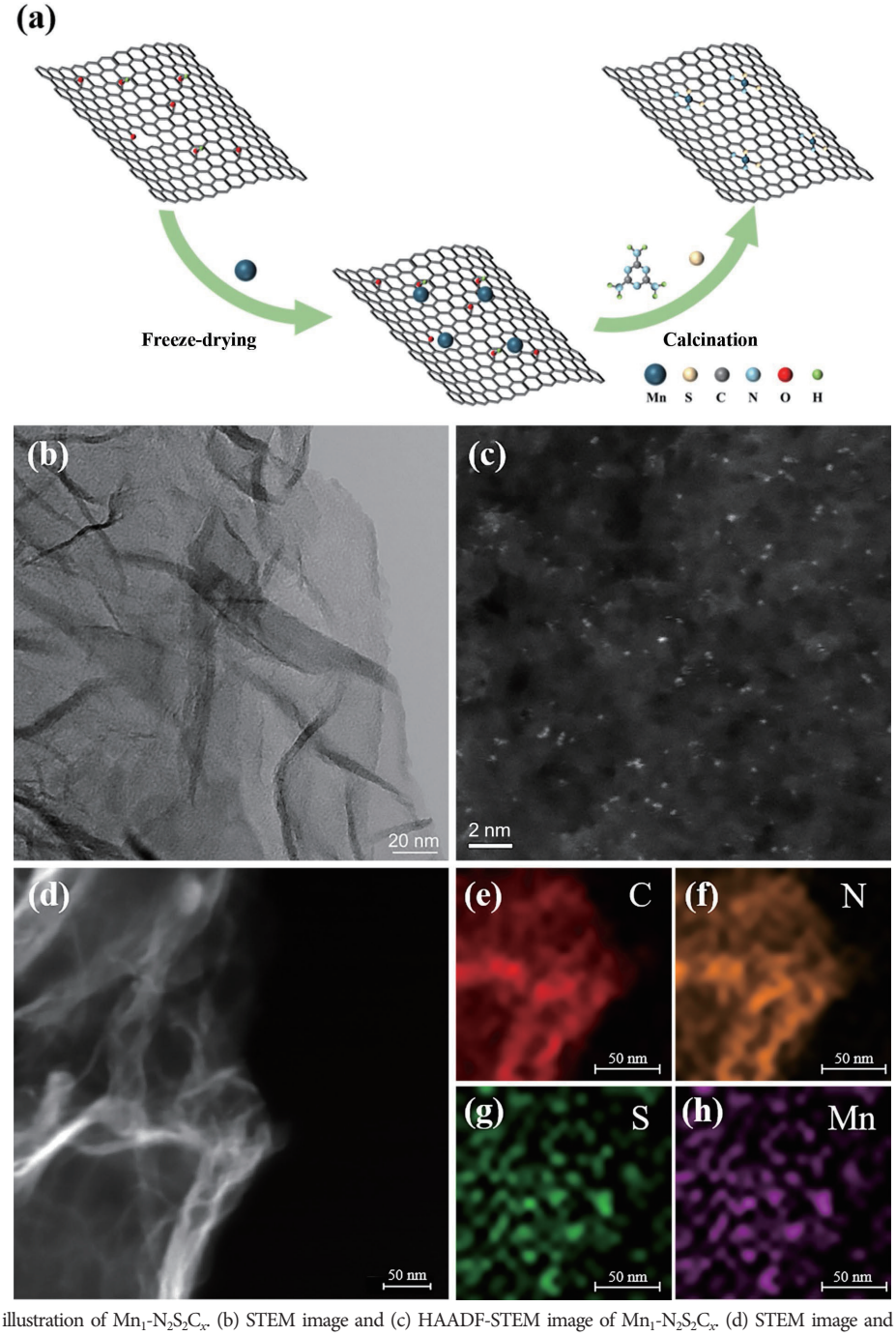

Figure 1 (a) Synthetic illustration of Mn_1-$N_2S_2C_x$. (b) STEM image and (c) HAADF-STEM image of Mn_1-$N_2S_2C_x$. (d) STEM image and ((e)–(h)) EDS elemental maps of Mn_1-$N_2S_2C_x$.

of these synthesized catalysts was analyzed by X-ray diffraction (XRD) (Fig. S1 in the Electronic Supplementary Material (ESM)), and the results show that no Mn nanoparticles exist on the catalysts synthesized by the annealing method. Moreover, annealing treatment did not damage the structure of graphene, proved by the wide peak at 26.5° [29, 30]. The morphology of samples was analyzed by scanning transmission electron microscopy (STEM) and high-angle annular dark field-STEM (HADDF-STEM) (Figs. 1(b) and 1(c)). The STEM image of Mn_1-$N_2S_2C_x$ is similar to that of graphene, indicating that the two-dimensional thin layer structure is inherited from graphene. The bright spots in the HAADF-STEM image indicate that Mn single atoms are successfully loaded onto the graphene, in the form of isolated single atoms rather than clusters. Energy dispersive X-ray spectra (EDS) elemental maps further demonstrate the uniform dispersion of Mn, N, and S elements (Figs. 1(d)–1(h)). The Brunauer–Emmett–Teller (BET) specific surface area of Mn_1-$N_2S_2C_x$ was measured to be 477 $m^2 \cdot g^{-1}$ (Fig. S2 in the ESM).

The valence states of single Mn atoms and composition in Mn_1-$N_2S_2C_x$ have been studied by X-ray photoelectron spectroscopy (XPS) and X-ray absorption fine structure (XAFS). The XPS results display that the atomic contents of Mn, N, and S in the Mn_1-$N_2S_2C_x$ are 1.03%, 5.85%, and 3.22%, respectively (Table S1 in the ESM). Further analysis of the chemical environment of Mn was performed with the help of XAFS. In the X-ray absorption near edge structure (XANES) spectra, the Mn K edge absorption of Mn_1-$N_2S_2C_x$ is slightly positive to that of MnO with a smaller edge energy than Mn_3O_4 and MnO_2, indicating that the doping of N/S increases the oxidation state of Mn (Fig. 2(a)) [31–33]. In the Fourier transform (FT) extended X-ray absorption fine structure (EXAFS) spectra, Mn_1-$N_2S_2C_x$ shows two prominent peaks, namely Mn–N scattering at 1.61 Å and Mn–S scattering at 2.16 Å (Fig. 2(b)). In addition, the scattering characteristic peaks of Mn–Mn and Mn–O in Mn foil and Mn_3O_4 are not observed in Mn_1-$N_2S_2C_x$, further proving atomic dispersed state of Mn species. Furthermore, the FT-EXAFS curve was fitted to quantify the coordination of Mn with N and S (Fig. 2(c)). The best fitting results uncover that the bond lengths of Mn–N and Mn–S are 1.88 ± 0.03 and 2.24 ± 0.04 Å, respectively, and the coordination numbers are 2.3 ± 0.5 and 1.7 ± 0.5. Different from the reported symmetric Mn-N_4 structure, the optimized structural model is Mn_1-N_2S_2, where the presence of S causes the distortion of the surroundings of Mn (Fig. 2(d)) [34].

2.2 OER performance

To investigate the influence of coordination environment of isolated Mn sites on the OER activity, the Mn-C, Mn-SC, Mn-NC and Mn_1-$N_2S_2C_x$ were tested in 1 M KOH and commercial IrO_2 was used for comparison. As depicted in Fig. 3(a), the overpotential (η_{10}) of Mn_1-$N_2S_2C_x$ is 280 mV, much smaller than that for Mn-C (407 mV), Mn-SC (372 mV), and Mn-NC (373 mV) and even lower than that of 294 mV for IrO_2. To achieve insights into the OER kinetics, Tafel slopes were investigated (Fig. 3(b)). The Mn_1-$N_2S_2C_x$ exhibits a low slope of 44 $mV \cdot dec^{-1}$, which is smaller than that of Mn-C (83 $mV \cdot dec^{-1}$), Mn-SC (66 $mV \cdot dec^{-1}$), and Mn-NC (81 $mV \cdot dec^{-1}$) and is close to that of IrO_2 (43 $mV \cdot dec^{-1}$), indicating that the OER kinetics has been greatly improved after N- and S-coordination to Mn sites. Moreover, the Tafel slope implies the second electron transfer being the rate-determining step on the Mn_1-$N_2S_2C_x$ [35]. The OER performance of Mn_1-$N_2S_2C_x$ surpasses most single-atom electrocatalysts reported so far (Fig. 3(c) and Table S2 in the ESM). For example, Ni-SAs@NC (η_{10} = 390 mV) [36], Mn SAC (η_{10} = 350 mV) [37], Fe-NiNC-50 (η_{10} = 340 mV) [38], Hb/BCNT-1000 (η_{10} = 326 mV) [39], 5%W-CCH (η_{10} = 318 mV) [40], and Ni-FePS3 NSs/C (η_{10} = 287 mV) [41]. The electrochemical double-layer capacitance (C_{dl}) analysis of the catalysts shows that the introduction of Mn atoms on graphene significantly increases the electrochemical active surface area (ECSA) (Figs. S3–S6 in the ESM). The ECSA of Mn_1-$N_2S_2C_x$ is 282 cm^2, much higher than that of M–NC (135 cm^2), Mn–SC (183 cm^2), and M–C (172.5 cm^2). In addition, the electron transfer rate is evaluated by the electrochemical impedance

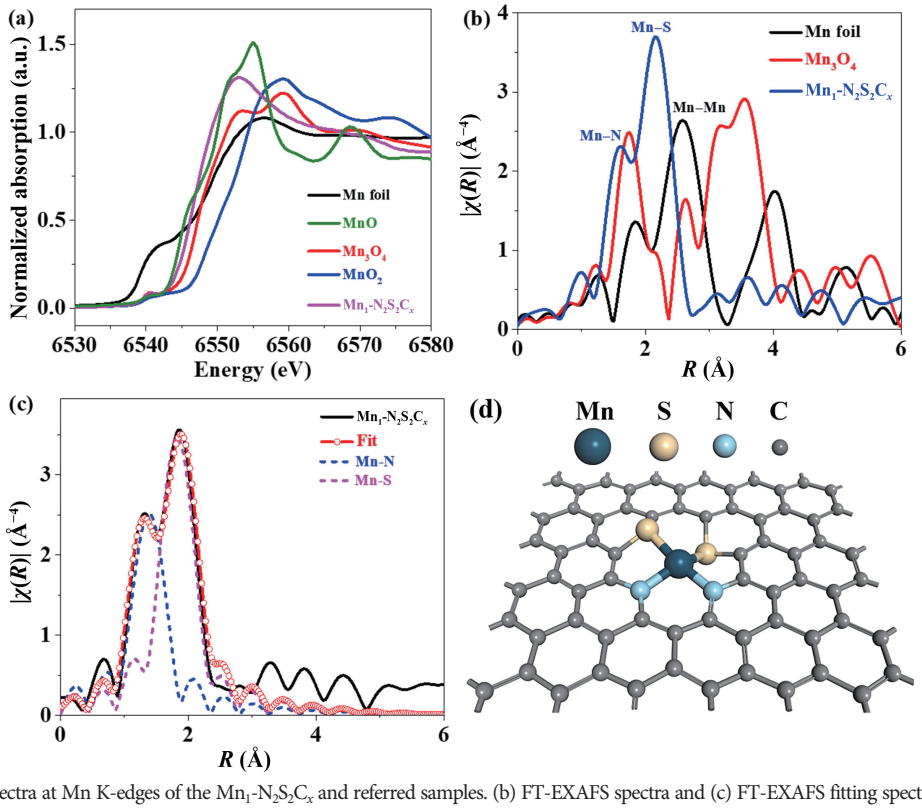

Figure 2 (a) XANES spectra at Mn K-edges of the Mn_1-$N_2S_2C_x$ and referred samples. (b) FT-EXAFS spectra and (c) FT-EXAFS fitting spectra. (d) Ortho-MnN_2S_2-G configuration.

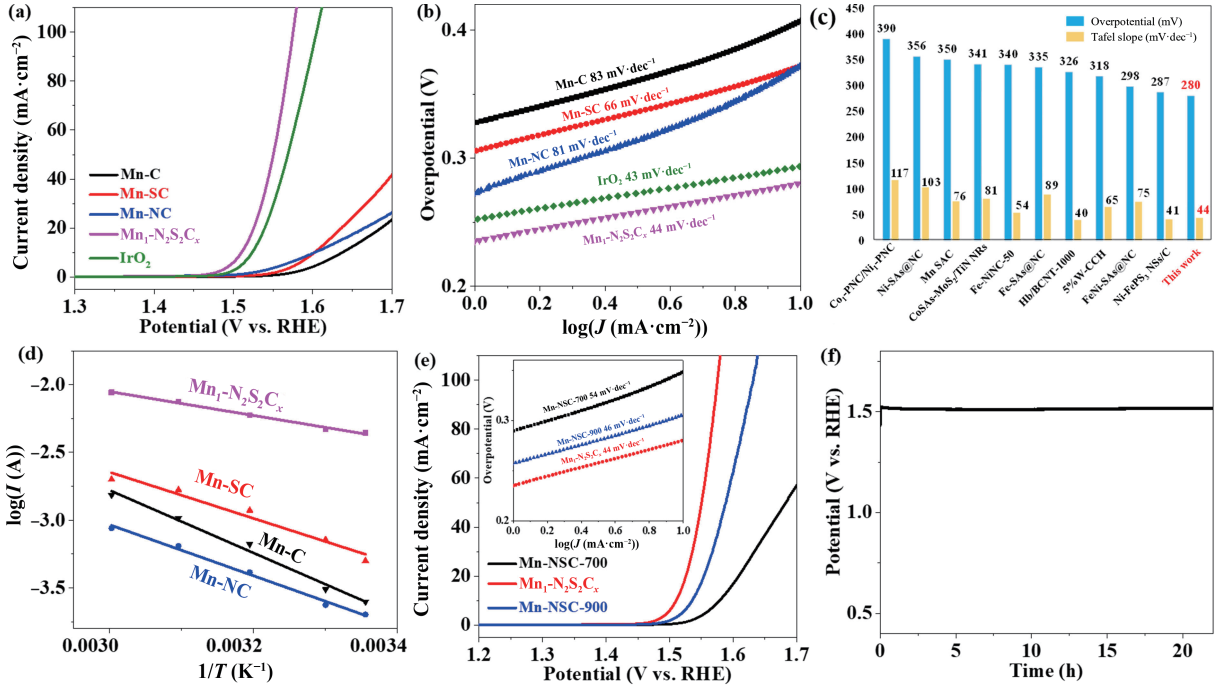

Figure 3 (a) OER polarization curves of Mn-C, Mn-SC, Mn-NC, Mn_1-$N_2S_2C_x$, and IrO_2, and (b) the corresponding Tafel slopes. (c) Comparisons of the η_{10} and Tafel slopes. (d) Arrhenius plots of the kinetic current at η = 300 mV. (e) OER polarization curves of Mn_1-$N_2S_2C_x$ annealed at different temperatures (inset: Tafel slopes). (f) Chronopotentiometric test for the Mn_1-$N_2S_2C_x$.

spectroscopy (EIS) spectra (Fig. S7 in the ESM), and the results display that Mn_1-$N_2S_2C_x$ has the smallest charge transfer resistance (3.6 Ω·cm²). The OER kinetics on Mn-C, Mn-SC, Mn-NC, and Mn_1-$N_2S_2C_x$ were further investigated by temperature-dependent electrocatalytic activity. As demonstrated in Fig. S8 in the ESM, the OER activity increases with the raising temperature. The OER activation energy (E_a) can be obtained using Arrhenius equation [42, 43]. By collecting the kinetic current at η = 300 mV, the E_a on the Mn_1-$N_2S_2C_x$ is calculated to be only 16.9 kJ·mol⁻¹, far lower than that on the Mn-C (44.3 kJ·mol⁻¹), Mn-SC (32.7 kJ·mol⁻¹), and Mn-NC (36.1 kJ·mol⁻¹), further revealing that N- and S-coordination to Mn sites can significantly lower the reaction energy barrier (Fig. 3(d)). The influence of annealing temperature on the OER activity of Mn_1-$N_2S_2C_x$ was studied. As displayed in Fig. 3(e), the Mn_1-$N_2S_2C_x$ annealed at 800 °C shows better OER performance than those annealed at 700 and 900 °C, which might be ascribed to different configurations of active sites generated at different temperatures [44, 45]. The different N- and S-coordination to Mn sites will significantly influence the OER activity as revealed by the following theoretical calculations. Stability is the key point to assess the feasibility of practical application, especially for single-atom catalysts. The long-term stability of Mn_1-$N_2S_2C_x$ was assessed by chronopotentiometric test at 10 mA·cm⁻². As exhibited in Fig. 3(f), the potential maintains almost constant within 22 h, indicating excellent stability of Mn_1-$N_2S_2C_x$ during the OER.

The Mn_1-$N_2S_2C_x$ after OER was characterized by TEM, XRD, and XPS to study the structural stability. The TEM image of Mn_1-$N_2S_2C_x$ reveals that no obvious structural changes during the OER process (Fig. S9 in the ESM). The XRD pattern of Mn_1-$N_2S_2C_x$ after OER test illustrates that the catalyst maintains single-atom structure without the formation of manganese nanoparticles and oxides (Fig. S10 in the ESM). XPS spectra of Mn_1-$N_2S_2C_x$ after OER test illustrate the existence of C, O, N, S, and Mn elements (Fig. 4(a)). The C 1s peak is weakened after the stability test, which is mainly attributed to the adsorption of water on the sample surface. The binding energy of Mn $2p_{3/2}$ in Mn_1-$N_2S_2C_x$-after OER (642.8 eV) is slightly higher than that of Mn_1-$N_2S_2C_x$ (643.1 eV), indicating that the content of high-oxidation-state Mn species increases due to the formation of Mn–O bond as revealed by the following theoretical calculations (Fig. 4(b)) [46]. The N 1s spectra show that five kinds of different nitrogen species (Mn–N, graphite nitrogen, nitrogen oxides, pyridine nitrogen, and pyrrole nitrogen) exist, in which pyridine N dominates (Fig. 4(c)) [47]. Additionally, the relative content of peak located at 399.0 eV keeps almost constant for the Mn_1-$N_2S_2C_x$ before and after OER, indicating that the content of Mn–N is not reduced during the OER. Similarly, the high-resolution S 2p spectra are deconvoluted into Mn–S, and S–C, and S–O species (Fig. 4(d)) [48, 49].

2.3 DFT calculations for different types of Mn_1-$N_xS_xC_x$

To explore the catalytic property difference of Mn_1-$N_xS_xC_x$ at the atomic level, density functional theory (DFT) calculations were carried out for the five catalytic systems, i.e., Mn_1-N_4C_x, Mn_1-N_3SC_x, para-Mn_1-$N_2S_2C_x$, ortho-Mn_1-$N_2S_2C_x$, and Mn_1-NS_3C_x. After screening by the energy evaluation, the five Mn-N_xS_xG models were established and optimized (Fig. 5 and Fig. S11 in the ESM). The results show that the catalytic sites of Mn_1-N_3SC_x, Mn_1-$N_2S_2C_x$, and Mn_1-NS_3C_x are nonplanar symmetric except for Mn_1-N_4C_x, due to the sulfur atom doping. The structures of Mn_1-N_4C_x and Mn_1-N_3SC_x are consistent with our previous work [46]. As for Mn_1-$N_2S_2C_x$, given the position of two sulfur atoms, two structures of Mn_1-$N_2S_2C_x$ were optimized, namely ortho-Mn_1-$N_2S_2C_x$ and para-Mn_1-$N_2S_2C_x$. Subsequently, the reaction channels for the OER and the intermediates are identified as the following: * + H_2O → OH* → O* → OOH* → * + O_2, as shown in Fig. 5 and Fig. S11 in the ESM. As the energy of OH* is lower than that of O* and OOH*, OH* is considered as the stable intermediate upon the absorption of OH, implying that these five catalytic systems are all exothermic in this step. However, the generation of O* on the five catalytic surfaces exhibits the significant energy difference. Among these five catalytic surfaces, Mn-N_4G and Mn-NS_3G have the high energy barriers to generate O*, with the barriers of 0.54 and 0.86 eV. As a result, the transformation from OH* to O* serves as the rate-limiting step for Mn_1-N_4C_x and Mn_1-NS_3C_x. In the following step, except for Mn_1-NS_3C_x, the formation of OOH*

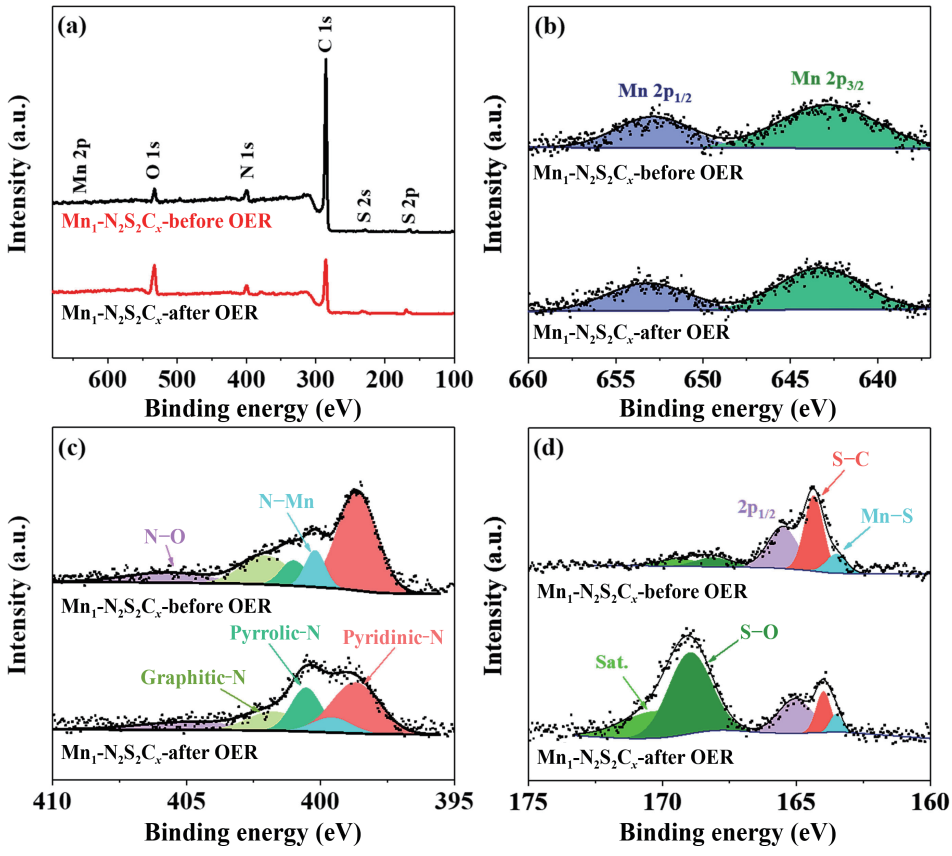

Figure 4 (a) XPS survey spectra of Mn_1-$N_2S_2C_x$ before and after OER. High-resolution XPS spectra of (b) Mn 2p, (c) N 1s, and (d) S 2p.

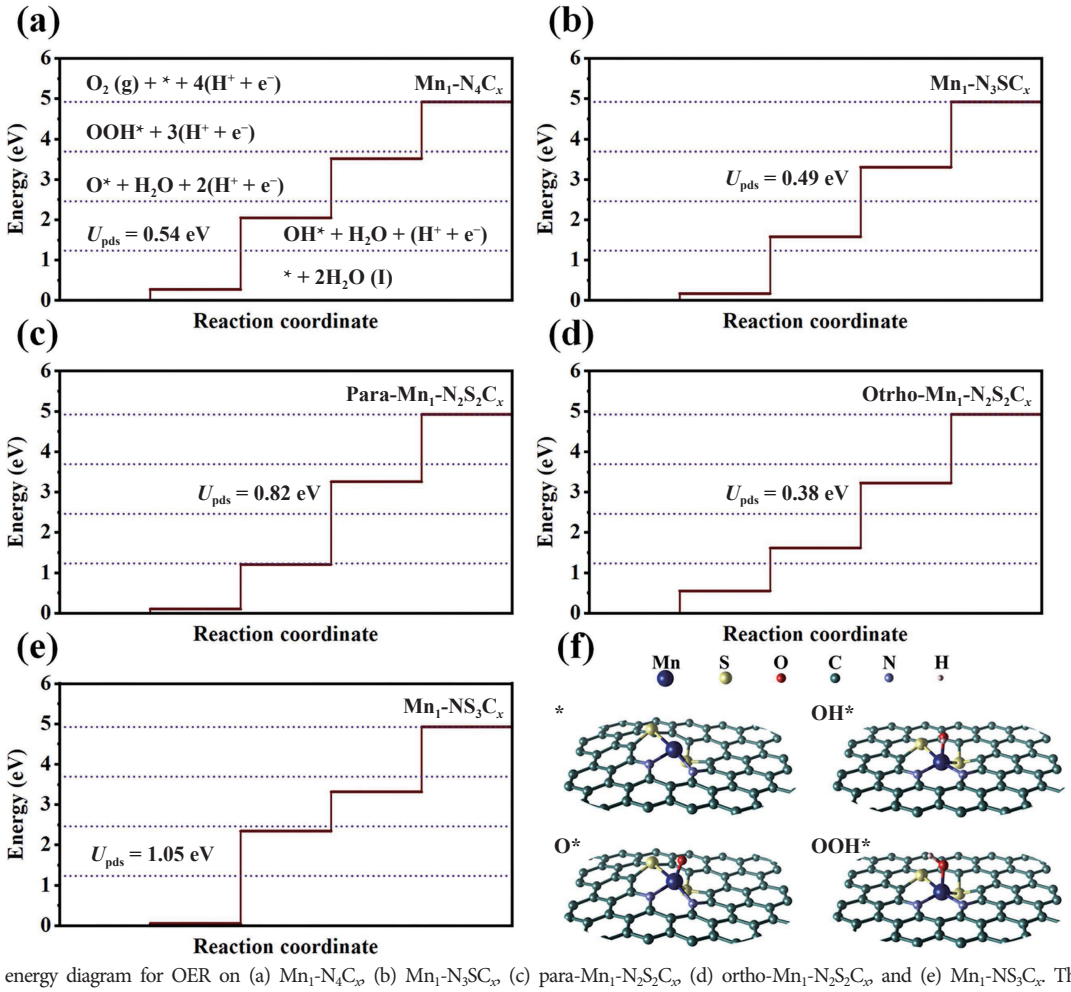

Figure 5 Free energy diagram for OER on (a) Mn_1-N_4C_x, (b) Mn_1-N_3SC_x, (c) para-Mn_1-$N_2S_2C_x$, (d) ortho-Mn_1-$N_2S_2C_x$, and (e) Mn_1-NS_3C_x. The dashed lines represent the step-free energy for an ideal electrocatalyst. (f) The optimized surface intermediate structures of ortho-Mn_1-$N_2S_2C_x$.

on the catalytic surfaces are still endothermic reactions, and Mn_1-N_3SC_x, ortho-Mn_1-$N_2S_2C_x$, and para-Mn_1-$N_2S_2C_x$ have the energy barriers of 0.49, 0.38, and 0.82 eV, respectively. In the OER process, the highest potential barrier determines that the rate-limiting step on Mn_1-N_3SC_x, ortho-Mn_1-$N_2S_2C_x$, and para-Mn_1-$N_2S_2C_x$ is O* → OOH*. Therefore, it is demonstrated that the ortho-Mn_1-$N_2S_2C_x$ could catalyse the OER with the lowest energy barrier, which is in line with the experimental results.

In addition, the projected density-of-states of Mn_1-N_4C_x, Mn_1-N_3SC_x, ortho-Mn_1-$N_2S_2C_x$, para-Mn_1-$N_2S_2C_x$, and Mn_1-NS_3C_x were analyzed to explore the modulation of the energy band structures of the catalytic surfaces by doping S atoms (Fig. 6). The results show that the conduction band and valence band of five modes could overlap with the Fermi level. Due to the sulfur atom doping, the work function of ortho-Mn_1-$N_2S_2C_x$ is higher than those of other four models, leading to the lower overpotential and higher catalytic activity. Furthermore, DFT calculations also show that due to the sulfur atom doping, the electron density of Mn increases compared with Mn_1-N_4C_x, particularly for ortho-Mn_1-$N_2S_2C_x$. In summary, the S atom doping, as well as asymmetry of structure leads to the higher catalytic activity of ortho-Mn_1-$N_2S_2C_x$.

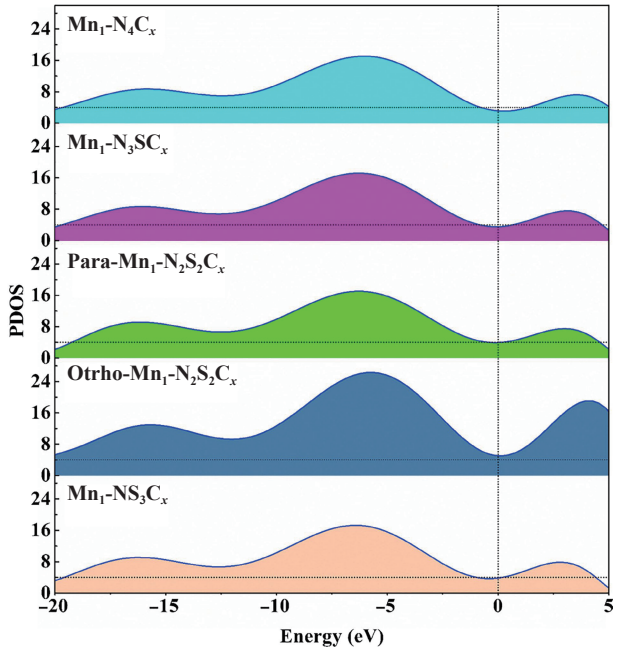

Figure 6 DFT-calculated projected density-of-states for the five catalytic modes.

3 Conclusions

In summary, we have successfully improved the OER activity of Mn-SACs through nitrogen and sulfur dual-heteroatom doping to adjust the coordinate structure of Mn atom. The Mn_1-$N_2S_2C_x$ synthesized by high-temperature annealing displays low OER overpotential (280 mV) and Tafel slope (44 mV·dec^{-1}). The excellent OER activity roots in the improved electron allocation of Mn and the asymmetric non-planar structure, which reduces the reaction barrier of the rate-limiting step. The optimization strategy for adjusting the electronic structure of M-N-C by introducing sulfur species provides possibilities for the development of highly efficient SACs for energy-related applications.

Acknowledgements

This work was supported by the National Natural Science Foundation of China (No. 22075099), the Natural Science Foundation of Jilin Province (No. 20220101051JC), and the Education Department of Jilin Province (No. JJKH20220967KJ)

Electronic Supplementary Material: Supplementary material (additional STEM, XRD patterns, BET data, electrochemical characterizations, and theoretical models) is available in the online version of this article at https://doi.org/10.1007/s12274-023-5859-8.

References

[1] Wang, D. W.; Li, Q.; Han, C.; Xing, Z. C.; Yang, X. R. Single-atom ruthenium based catalyst for enhanced hydrogen evolution. *Appl. Catal. B:Environ.* **2019**, *249*, 91–97.

[2] Meng, X. D.; Liu, X.; Fan, X. Y.; Chen, X.; Chen, S.; Meng, Y. Q.; Wang, M. Y.; Zhou, J.; Hong, S.; Zheng, L. et al. Single-atom catalyst aggregates: Size-matching is critical to electrocatalytic performance in sulfur cathodes. *Adv. Sci.* **2022**, *9*, 2103773.

[3] Yin, P. Q.; You, B. Atom migration-trapping toward single-atom catalysts for energy electrocatalysis. *Mater. Today Energy* **2021**, *19*, 100586.

[4] Li, Y.; Wang, H. H.; Priest, C.; Li, S. W.; Xu, P.; Wu, G. Advanced electrocatalysis for energy and environmental sustainability via water and nitrogen reactions. *Adv. Mater.* **2021**, *33*, 2000381.

[5] Suen, N. T.; Hung, S. F.; Quan, Q.; Zhang, N.; Xu, Y. J.; Chen, H. M. Electrocatalysis for the oxygen evolution reaction: Recent development and future perspectives. *Chem. Soc. Rev.* **2017**, *46*, 337–365.

[6] Huang, Z. F.; Song, J. J.; Dou, S.; Li, X. G.; Wang, J.; Wang, X. Strategies to break the scaling relation toward enhanced oxygen electrocatalysis. *Matter* **2019**, *1*, 1494–1518.

[7] Tahir, M.; Pan, L.; Idrees, F.; Zhang, X. W.; Wang, L.; Zou, J. J.; Wang, Z. L. Electrocatalytic oxygen evolution reaction for energy conversion and storage: A comprehensive review. *Nano Energy* **2017**, *37*, 136–157.

[8] Zhang, F. F.; Cheng, C. Q.; Wang, J. Q.; Shang, L.; Feng, Y.; Zhang, Y.; Mao, J.; Guo, Q. J.; Xie, Y. M.; Dong, C. K. et al. W. Iridium oxide modified with silver single atom for boosting oxygen evolution reaction in acidic media. *ACS Energy Lett.* **2021**, *6*, 1588–1595.

[9] Tian, L.; Li, Z.; Xu, X. N.; Zhang, C. Advances in noble metal (Ru, Rh, and Ir) doping for boosting water splitting electrocatalysis. *J. Mater. Chem. A* **2021**, *9*, 13459–13470.

[10] Yi, D.; Lu, F.; Zhang, F. C.; Liu, S. J.; Zhou, B.; Gao, D. L.; Wang, X.; Yao, J. N. Regulating charge transfer of lattice oxygen in single-atom-doped titania for hydrogen evolution. *Angew. Chem., Int. Ed.* **2020**, *59*, 15855–15859.

[11] Zhu, Y. Z.; Peng, W. C.; Li, Y.; Zhang, G. L.; Zhang, F. B.; Fan, X. B. Modulating the electronic structure of single-atom catalysts on 2D nanomaterials for enhanced electrocatalytic performance. *Small Methods* **2019**, *3*, 1800438.

[12] Maiti, K.; Maiti, S.; Curnan, M. T.; Kim, H. J.; Han, J. W. Engineering single atom catalysts to tune properties for electrochemical reduction and evolution reactions. *Adv. Energy Mater.* **2021**, *11*, 2101670.

[13] Rao, P.; Wu, D. X.; Wang, T. J.; Li, J.; Deng, P. L.; Chen, Q.; Shen, Y. J.; Chen, Y.; Tian, X. L. Single atomic cobalt electrocatalyst for efficient oxygen reduction reaction. *eScience* **2022**, *2*, 399–404.

[14] Rao, P.; Wang, T. J.; Li, J.; Deng, P. L.; Shen, Y. J.; Chen, Y.; Tian, X. L. Plasma induced Fe-N_x active sites to improve the oxygen reduction reaction performance. *Adv. Sensor Energy Mater.* **2022**, *1*, 100005.

[15] Xu, H. X.; Cheng, D. J.; Cao, D. P.; Zeng, X. C. A universal principle for a rational design of single-atom electrocatalysts. *Nat. Catal.* **2018**, *1*, 339–348.

[16] Lu, T. T.; Wang, H. Graphdiyne-supported metal electrocatalysts: From nanoparticles and cluster to single atoms. *Nano Res.* **2022**, *15*, 9764–9778.

[17] Feng, J. Q.; Gao, H. S.; Zheng, L. R.; Chen, Z. P.; Zeng, S. J.; Jiang, C. Y.; Dong, H. F.; Liu, L. C.; Zhang, S. J.; Zhang, X. P. A Mn-N_3

single-atom catalyst embedded in graphitic carbon nitride for efficient CO_2 electroreduction. *Nat. Commun.* **2020**, *11*, 4341.
[18] Yang, Y.; Mao, K. T.; Gao, S. Q.; Huang, H.; Xia, G. L.; Lin, Z. Y.; Jiang, P.; Wang, C. L.; Wang, H.; Chen, Q. W. O-, N-atoms-coordinated Mn cofactors within a graphene framework as bioinspired oxygen reduction reaction electrocatalysts. *Adv. Mater.* **2018**, *30*, 1801732.
[19] Zhao, C. X.; Liu, J. N.; Wang, J.; Wang, C. D.; Guo, X.; Li, X. Y.; Chen, X.; Song, L.; Li, B. Q.; Zhang, Q. A clicking confinement strategy to fabricate transition metal single-atom sites for bifunctional oxygen electrocatalysis. *Sci. Adv.,* **2020**, *8*, eabn5091.
[20] Rong, X.; Wang, H. J.; Lu, X. L.; Si, R.; Lu, T. B. Controlled synthesis of a vacancy-defect single-atom catalyst for boosting CO_2 electroreduction. *Angew. Chem., Int. Ed.* **2020**, *59*, 1961–1965.
[21] Li, L.; Chen, Y. J.; Xing, H. R.; Li, N.; Xia, J. W.; Qian, X. Y.; Xu, H.; Li, W. Z.; Yin, F. X.; He, G. Y. et al. Single-atom Fe-N_5 catalyst for high-performance zinc-air batteries. *Nano Res.* **2022**, *15*, 8056–8064.
[22] Peng, L. S.; Yang, J.; Yang, Y. Q.; Qian, F. R.; Wang, Q.; Sun-Waterhouse, D.; Shang, L.; Zhang, T. R.; Waterhouse, G. I. N. Mesopore-rich Fe-N-C catalyst with FeN_4-O-NC single-atom sites delivers remarkable oxygen reduction reaction performance in alkaline media. *Adv. Mater.* **2022**, *34*, 2202544.
[23] Lin, W. J.; Lu, Y. R.; Peng, W.; Luo, M.; Chan, T. S.; Tan, Y. W. Atomic bridging modulation of Ir-N, S co-doped MXene for accelerating hydrogen evolution. *J. Mater. Chem. A* **2022**, *10*, 9878–9885.
[24] Hwang, J.; Noh, S. H.; Han, B. Design of active bifunctional electrocatalysts using single atom doped transition metal dichalcogenides. *Appl. Surf. Sci.* **2019**, *471*, 545–552.
[25] Su, P. P.; Pei, W.; Wang, X. W.; Ma, Y. F.; Jiang, Q. K.; Liang, J.; Zhou, S.; Zhao, J. J.; Liu, J.; Lu, G. Q. Exceptional electrochemical HER performance with enhanced electron transfer between Ru nanoparticles and single atoms dispersed on a carbon substrate. *Angew. Chem., Int. Ed.* **2021**, *60*, 16044–16050.
[26] Zhu, P.; Xiong, X.; Wang, D. S. Regulations of active moiety in single atom catalysts for electrochemical hydrogen evolution reaction. *Nano Res.* **2022**, *15*, 5792–5815.
[27] Gu, J. X.; Magagula, S.; Zhao, J. X.; Chen, Z. F. Boosting ORR/OER activity of graphdiyne by simple heteroatom doping. *Small Methods* **2019**, *3*, 1800550.
[28] Wang, M. W.; Cao, L.; Du, X.; Zhang, Y.; Jin, F. B.; Zhang, M. L.; Li, Z. H.; Su, K. M. Highly dispersed Co-, N-, S-doped topological defect-rich hollow carbon nanoboxes as superior bifunctional oxygen electrocatalysts for rechargeable Zn-air batteries. *ACS Appl. Mater. Interfaces* **2022**, *14*, 25427–25438.
[29] Ruammaitree, A.; Nakahara, H.; Akimoto, K.; Soda, K.; Saito, Y. Determination of non-uniform graphene thickness on SiC(0001) by X-ray diffraction. *Appl. Surf. Sci.* **2013**, *282*, 297–301.
[30] Seehra, M. S.; Narang, V.; Geddam, U. K.; Stefaniak, A. B. Correlation between X-ray diffraction and Raman spectra of 16 commercial grapheme-based materials and their resulting classification. *Carbon* **2017**, *111*, 380–385.
[31] Schnegg, A.; Nehrkorn, J.; Singh, A.; Calafell, I. A.; Bonke, S. A.; Hocking, R. K.; Lips, K.; Spiccia, L. Probing the fate of Mn complexes in nafion: A combined multifrequency EPR and XAS study. *J. Phys. Chem. C* **2016**, *120*, 853–861.
[32] Colmer, H. E.; Howcroft, A. W.; Jackson, T. A. Formation, characterization, and O–O bond activation of a peroxomanganese(III) complex supported by a cross-clamped cyclam ligand. *Inorg. Chem.* **2016**, *55*, 2055–2069.
[33] He, M. R.; Li, X. J.; Liu, Y. H.; Li, J. F. Axial Mn–C_{CN} bonds of cyano manganese(II) porphyrin complexes: Flexible and weak. . *Inorg. Chem.* **2016**, *55*, 5871–5879.
[34] Guan, J. Q.; Duan, Z. Y.; Zhang, F. X.; Kelly, S. D.; Si, R.; Dupuis, M.; Huang, Q. E.; Chen, J. Q.; Tang, C. H.; Li, C. Water oxidation on a mononuclear manganese heterogeneous catalyst. *Nat. Catal.* **2018**, *1*, 870–877.
[35] Guan, J. Q.; Bai, X.; Tang, T. M. Recent progress and prospect of carbon-free single-site catalysts for the hydrogen and oxygen evolution reactions. *Nano Res.* **2022**, *15*, 818–837.
[36] Hu, B. T.; Huang, A. J.; Zhang, X. J.; Chen, Z.; Tu, R. Y.; Zhu, W.; Zhuang, Z. B.; Chen, C.; Peng, Q.; Li, Y. D. Atomic Co/Ni dual sites with N/P-coordination as bifunctional oxygen electrocatalyst for rechargeable zinc-air batteries. *Nano Res.* **2021**, *14*, 3482–3488.
[37] Shang, H. S.; Sun, W. M.; Sui, R.; Pei, J. J.; Zheng, L. R.; Dong, J. C.; Jiang, Z. L.; Zhou, D. N.; Zhuang, Z. B.; Chen, W. X. et al. Engineering isolated Mn-N_2C_2 atomic interface sites for efficient bifunctional oxygen reduction and evolution reaction. *Nano Lett.* **2020**, *20*, 5443–5450.
[38] Zhu, X. F.; Zhang, D. T.; Chen, C. J.; Zhang, Q. R.; Liu, R. S.; Xia, Z. H.; Dai, L. M.; Amal, R.; Lu, X. Y. Harnessing the interplay of Fe-Ni atom pairs embedded in nitrogen-doped carbon for bifunctional oxygen electrocatalysis. *Nano Energy* **2020**, *71*, 104597.
[39] Chen, W. M.; Luo, X. L.; Ling, S. L.; Zhou, Y. F.; Shen, B. H.; Slater, T. J. A.; Fernandes, J. A.; Lin, T. T.; Wang, J. S.; Shen, Y. Hemoglobin-derived Fe-N_x-S species supported by bamboo-shaped carbon nanotubes as efficient electrocatalysts for the oxygen evolution reaction. *Carbon* **2020**, *168*, 588–596.
[40] Jin, M. M.; Li, J. W.; Gao, J. C.; Liu, W. L.; Han, J.; Liu, H. M.; Zhan, D.; Lai, L. F. Atomic-level tungsten doping triggered low overpotential for electrocatalytic water splitting. *J. Colloid Interface Sci.* **2021**, *587*, 581–589.
[41] Tang, C. Y.; He, D.; Zhang, N.; Song, X. Y.; Jia, S. F.; Ke, Z. J.; Liu, J. C.; Wang, J. B.; Jiang, C. Z.; Wang, Z. Y. et al. Electronic coupling of single atom and $FePS_3$ boosts water electrolysis. *Energy Environ. Mater.* **2022**, *5*, 899–905.
[42] Bai, X.; Duan, Z. Y.; Nan, B.; Wang, L. M.; Tang, T. M.; Guan, J. Q. Unveiling the active sites of ultrathin Co-Fe layered double hydroxides for the oxygen evolution reaction. *Chin. J. Catal.* **2022**, *43*, 2240–2248.
[43] Swierk, J. R.; Klaus, S.; Trotochaud, L.; Bell, A. T.; Tilley, T. D. Electrochemical study of the energetics of the oxygen evolution reaction at nickel iron (Oxy)hydroxide catalysts. *J. Phys. Chem. C* **2015**, *119*, 19022–19029.
[44] Yin, P. Q.; Yao, T.; Wu, Y. E.; Zheng, L. R.; Lin, Y.; Liu, W.; Ju, H. X.; Zhu, J. F.; Hong, X.; Deng, Z. X. et al. Single cobalt atoms with precise N-coordination as superior oxygen reduction reaction catalysts. *Angew. Chem., Int. Ed.* **2016**, *55*, 10800–10805.
[45] Han, L. L.; Cheng, H.; Liu, W.; Li, H. Q.; Ou, P. F.; Lin, R. Q.; Wang, H. T.; Pao, C. W.; Head, A. R.; Wang, C. H. et al. A single-atom library for guided monometallic and concentration-complex multimetallic designs. *Nat. Mater.* **2022**, *21*, 681–688.
[46] Bai, X.; Wang, L. M.; Nan, B.; Tang, T. M.; Niu, X. D.; Guan, J. Q. Atomic manganese coordinated to nitrogen and sulfur for oxygen evolution. *Nano Res.* **2022**, *15*, 6019–6025.
[47] Guo, D.; Huang, Z.; Liu, Y. Y.; Zhang, Q.; Yang, Y. L.; Hong, J. M. Incorporation of single-atom copper into nitrogen-doped graphene for acetaminophen electrocatalytic degradation. *Appl. Surf. Sci.* **2022**, *604*, 154561.
[48] Liu, D. W.; Srinivas, K.; Chen, X.; Ma, F.; Zhang, X. J.; Wang, X. Q.; Wang, B.; Chen, Y. F. Dual Fe, Zn single atoms anchored on carbon nanotubes inlaid N, S-doped hollow carbon polyhedrons for boosting oxygen reduction reaction. *J. Colloid Interface Sci.* **2022**, *624*, 680–690.
[49] Lu, G. P.; Shan, H. B.; Lin, Y. M.; Zhang, K.; Zhou, B. J.; Zhong, Q.; Wang, P. C. A Fe single atom on N, S-doped carbon catalyst for performing N-alkylation of aromatic amines under solvent-free conditions. *J. Mater. Chem. A* **2021**, *9*, 25128–25135.